INT. J. NUM. METH. HEAT FLUID FLOW, VOL. 3, 357–375 (1993)

NUMERICAL ANALYSIS ON STROUHAL FREQUENCIES IN VORTEX SHEDDING OVER SQUARE CYLINDERS WITH SURFACE SUCTION AND BLOWING*

LISA M. LING, BALASUBRAMANIAM RAMASWAMY, RUBEN D. COHEN AND TSWEN-CHYUAN JUE

Department of Mechanical Engineering and Materials Science, Rice University, Houston, Texas 77251-1892, USA

ABSTRACT

The effects of normal surface suction and blowing on the Strouhal frequencies in vortex shedding over porous square cylinders was analysed numerically. The general characteristics determined were (1) an initial increase followed by a decreasing behaviour in the Strouhal frequency with increasing suction velocity and (2) a decrease in the Strouhal frequency with increasing blowing velocity. The numerical results were compared to an existing preliminary model, yielding fairly close agreement.

KEY WORDS Vortex shedding Surface suction and blowing Strouhal frequencies Navier–Stokes equations Finite element method

INTRODUCTION

The studies of vortex shedding over various structural shapes in the past have contributed to better understanding of areas such as aerodynamics and aeroelastic characteristics. This in turn will allow improved engineering designs much needed for better energy conservation of higher performance. Practical applications involve the design of automobiles, tall buildings, suspension bridges, heat exchangers, chimneys, etc.[1,2].

Abundant research had been done in the analysis of Strouhal frequencies (St) in vortex shedding over impermeable bodies. The analytical, numerical, and experimental results can be easily obtained in the publications of such work[1–10]. However, the Strouhal frequencies in vortex shedding over porous surfaces involving suction or blowing has not been widely researched. The only study found dealing directly with the problem were from the preliminary model of flows over porous cylinders by Cohen[11]. In this study, Cohen derived a model to predict the general effect of normal suction and blowing on the St–Re relationship.

The interest of this investigation is to numerically analyse the Strouhal frequencies in vortex shedding over porous square cylinders with various suction and blowing velocities. A comparison of the analytical and numerical solutions will help to assess the validity of the theoretical predictions and provide insights to the suction and blowing problem.

The finite element method used for this analysis is a fourth-order Runge–Kutta time integration scheme based on the Chorin's splitting scheme[12]. Three benchmark cases were examined to verify the numerical algorithm.

*This research was partially supported by National Science Foundation under grant DMS-9112847.

0961–5539/93/040357–19$2.00

Received November 1992

PRELIMINARY MODEL FOR PREDICTING THE EFFECTS OF SURFACE SUCTION AND BLOWING ON STROUHAL FREQUENCY

A simple model was derived by Cohen[11] to predict the general characteristics of vortex shedding over cylinders with surface suction and injection. The basis of this model is the assumption that the viscous length is directly proportional to the boundary layer thickness, δ. A brief summary of the derivation is given.

The model was first derived using scaling arguments to predict the characteristics of St for flow over a solid, circular cylinder with a radius R. In the interest of space, we shall forego the details of the derivation and refer the interested reader to Cohen[11]. The final results, however, are as follows:

$$St_{\text{suction}} \sim \frac{Re_0^2}{Re_\infty} \quad \text{when} \quad \frac{Re_0^2}{Re_\infty} \gg 1 \tag{1}$$

$$St_{\text{blowing}} \sim \frac{Re_\infty}{Re_0^2} \quad \text{when} \quad \frac{Re_0^2}{Re_\infty} \gg 1 \tag{2}$$

$$St_{\text{suction\&blowing}} \sim \text{constant} \quad \text{when} \quad \frac{Re_0^2}{Re_\infty} \ll 1 \tag{3}$$

where $Re_0 = v_0 d/\nu$, $Re_\infty = Ud/\nu$, U is the freestream velocity, v_0 is the suction or blowing velocity, ν is the fluid viscosity, and d is the cylinder diameter. These predicted results are shown graphically as in *Figure 1*. This Figure indicates that there exists a critical Re_∞, defined as:

$$Re_{\infty\,\text{critical}} = Re_0^2 \tag{4}$$

such that, if $Re_\infty \ll Re_{\infty\,\text{critical}}$, then the effects of suction or blowing must be accounted for. Else if $Re_\infty \gg Re_{\infty\,\text{critical}}$, then these effects become negligible, and the cylinder can be treated as impermeable. At the region where $Re_\infty \approx Re_{\infty\,\text{critical}} (Re_0^2/Re_\infty \approx 1)$, denoted by the broken lines in *Figure 1*, ΔSt should be less than $\pm 10\%$ or $\pm 20\%$. For systems operating at $Re_\infty \ll Re_{\infty\,\text{critical}}$, the predicted results also indicated that, on a log–log plot shown in *Figure 1*, the slopes of all the $St - Re_0^2/Re_\infty$ curves will asymptotically approach $+1$ for suction and -1 for blowing, for all suction and blowing velocities.

It was also mentioned by Cohen that there may exist an upper bound for the normal suction problem. As the suction velocity increases, the onset of flow separation may be delayed, and vortex shedding may become completely suppressed.

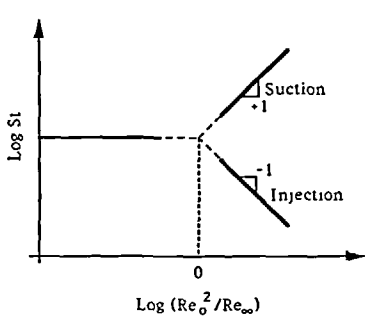

Figure 1 Analytical log St – log(Re_0^2/Re_∞) relationship

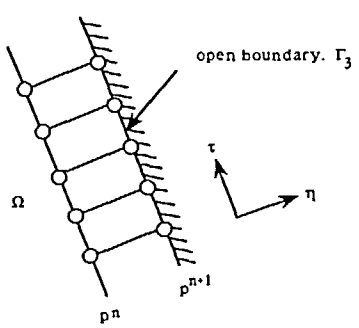

Figure 2 Outflow boundary condition

NUMERICAL APPROACH

The numerical algorithm used for this study was based on the explicit fourth order Runge–Kutta scheme[13]. In computing the solutions for flows past cylinders, a fixed perturbation was not imposed. It is the numerical noise which leads the symmetric flow into a vortex shedding state. The numerical noise is composed of discretization and roundoff errors[14].

Navier–Stokes equations

For an incompressible flow, the time-dependent Navier–Stokes equations are:

$$\frac{\partial \mathbf{u}}{\partial t}=\mathbf{u}\cdot\nabla\mathbf{u}=-\nabla p+\frac{1}{Re}\nabla^2\mathbf{u}+\mathbf{S} \tag{5}$$

$$\nabla\cdot\mathbf{u}=0 \tag{6}$$

Here $\mathbf{u}$ is the velocity vector, p the pressure; $Re=Ud/v$ the Reynolds number, where U, d are the characteristic velocity and length, respectively, v the kinematic viscosity; and S, a source term which represents external forces, such as gravity or electromagnetic force.

To complete the formulation, a set of boundary and initial conditions are required. The Dirichlet boundary condition for the velocity may be expressed as:

$$\mathbf{u}=\hat{\mathbf{u}} \text{ on } \Gamma_1 \tag{7}$$

where $\hat{\mathbf{u}}$ denotes the function that is given on the boundary, Γ_1.

The specified stress boundary condition can be expressed as:

$$\sigma\cdot\mathbf{n}=\hat{\sigma} \text{ on } \Gamma_2 \tag{8}$$

where $\hat{\sigma}$ is a specified stress function on the boundary Γ_2. $\Gamma=\Gamma_1\cup\Gamma_2$, is the boundary of the domain.

The outflow boundary Γ_3, which is a part of the boundary Γ_2 is shown in *Figure 2*, where the two right-most columns of the mesh are considered. Taking the normal and tangential derivatives of the Navier–Stokes equations and using the continuity equation, the pressure Poisson equation for the boundary can be obtained as:

$$\left(\frac{\partial^2}{\partial\eta^2}+\frac{\partial^2}{\partial\tau^2}\right)p^{n+1}=2\frac{\partial \mathbf{u}_\eta^n}{\partial\eta}\frac{\partial \mathbf{u}_\tau^n}{\partial\tau}-2\frac{\partial \mathbf{u}_\eta^n}{\partial\tau}\frac{\partial \mathbf{u}_\tau^n}{\partial\eta} \tag{9}$$

Dirichlet boundary condition is required to solve for (9). However, for the nodes on which Dirichlet boundary condition is given will remain the same forever and thus as time progresses the vortex will not shed. Therefore, to overcome the above difficulty, right-most columns of the mesh are used approximately. The integration of (9) for the last strip of elements as shown in *Figure 2* can be performed and it leads to the following set of equatiions:

$$[A]\begin{bmatrix}p^{n+1}\\ p^n\end{bmatrix}=\begin{bmatrix}\mathbf{q}^n\\ 0\end{bmatrix} \tag{10}$$

where p^{n+1} on Γ_3 are unknown, p^n on the adjacent nodes are known, A is the Laplacian matrix, $\mathbf{q}^n$ is the velocity gradient vector on the right hand side of (10). Thus, only the pressure at $t=0$ is needed to solve for (10). This approach was adopted by Shimura and Kawahara[4] using one step explicit velocity correction method.

Let the initial condition be given by:

$$\mathbf{u}(\mathbf{x},0)=\mathbf{u}_0(\mathbf{x}) \tag{11}$$

Then it is required that:

$$\mathbf{n}\cdot\mathbf{u}_0=\mathbf{n}\cdot\hat{\mathbf{u}} \tag{12}$$

and

$$\nabla\cdot\mathbf{u}_0=0 \tag{13}$$

in order that a solution exist. The above conditions are known as solvability conditions for the Navier–Stokes equations. Navier–Stokes equations are ill-posed if any of the above two conditions are violated[15].

Solving for pressure

Apart from the fact that Navier–Stokes equations are non-linear, the absence of pressure in the continuity equation in the case of incompressible flow poses the biggest problem. In compressible flow the time derivative of pressure appears in the continuity equation and evaluation of pressure does not pose as much challenge as it does in incompressible flows. Direct solution of $\mathbf{u}$ and p would require the approximating spaces satisfy the Babuska–Brezzi stability criteria. In order to satisfy the Babuska–Brezzi stability criteria the approximating spaces for the pressure are chosen to be of lower order than those used for velocities, i.e. staggered grids or mixed formulations need to be used.

However, if $\mathbf{u}$ and p are solved for in a decoupled manner, then we could obtain stable solution using both staggered and non-staggered grids[16]. There are two common formulations for the numerical solution of the incompressible Navier–Stokes equations in primitive variables, the artificial compressibility and the pressure Poisson equation method. The velocity field is calculated from the time dependent momentum equation using time marching techniques, while each method employs a different equation to compute the pressure. In the artificial compressibility method, a time derivative of the pressure is added to the continuity equation and the incompressible field is treated as compressible during transient calculations[17]. On the other hand, the pressure Poisson method replaces the continuity equation with a second-order elliptic Poisson equation for the pressure[18]. However, if artificial compressibility method is chosen then equal order approximations for pressure and velocity would require that a fourth order pressure derivative be added to the continuity equation to stabilize the solution. But no such stabilizing term is inherent in the procedure. We chose to use the pressure Poisson equation since it was felt that artificial compressibility method may impose a more stringent restriction on the time step.

Temporal discretization

The best approach to date for computing the time evolution of the Navier–Stokes equations is Chorin's time-step splitting technique.

In Chorin's approach explicit techniques are used to advance the velocity one time step while the new pressure is found by solving a linear partial differential equation. The first step is to predict the solution $\bar{\mathbf{u}}$ to (5) at the $(n+1)$th time step that would result if the pressure term were neglected. Replacing the time derivative by $(\bar{\mathbf{u}}^{n-1}-\mathbf{u}^n)/\Delta t$ gives:

$$\bar{\mathbf{u}}^{n+1}=\mathbf{u}^n+\Delta t\left(\frac{1}{Re}\nabla^2\mathbf{u}+\mathbf{S}-\mathbf{u}\cdot\nabla\mathbf{u}\right)^n \tag{14}$$

where the superscript n denotes the nth time step. The second step is to develop the pressure and corrected velocity fields that satisfy the continuity equation by using the relationships:

$$\mathbf{u}^{n+1}=\bar{\mathbf{u}}^{n-1}-\Delta t\nabla p \tag{15}$$

$$\nabla\cdot\mathbf{n}^{n+1}=0 \tag{16}$$

Note that the size of a stable time-step Δt can be increased by using an adaptation of Runge–Kutta techniques at the high Reynolds number and the Stokes solution at the low Reynolds number. An equation for the pressure can be obtained by taking the divergence of (15). In view of (16), one has:

$$\nabla^2 p = \frac{\nabla \cdot \bar{\mathbf{n}}^{n+1}}{\Delta t} \tag{17}$$

If p satisfies (17), then $\mathbf{u}^{n+1}$ does indeed satisfy (16). Based on the Chorin's projection method, the four stage Runge–Kutta method can be described as follows:

Stage 1:

$$\bar{\mathbf{u}}^{n+1(1)} = \mathbf{u}^n + \frac{\Delta t}{2}\left(\frac{1}{Re}\nabla^2 \mathbf{u} + \mathbf{S} - \mathbf{u}\cdot\nabla\mathbf{u}\right)^n \tag{18}$$

$$\nabla^2 p = 2\frac{\nabla \cdot \bar{\mathbf{u}}^{n+1(1)}}{\Delta t} \tag{19}$$

$$\mathbf{u}^{n+1(1)} = \bar{\mathbf{u}}^{n+1(1)} - \frac{\Delta t}{2}\nabla p \tag{20}$$

$$\nabla \cdot \mathbf{u}^{n+1(1)} = 0 \tag{21}$$

Stage 2:

$$\bar{\mathbf{u}}^{n+1(2)} = \mathbf{u}^n + \frac{\Delta t}{2}\left(\frac{1}{Re}\nabla^2 \mathbf{u} + \dot{\mathbf{S}} - \mathbf{u}\cdot\nabla\mathbf{u}\right)^{n+1(1)} \tag{22}$$

$$\nabla^2 p = 2\frac{\nabla \cdot \bar{\mathbf{u}}^{n+1(2)}}{\Delta t} \tag{23}$$

$$\mathbf{u}^{n+1(2)} = \bar{\mathbf{u}}^{n+1(2)} - \frac{\Delta t}{2}\nabla p \tag{24}$$

$$\nabla \cdot \mathbf{u}^{n+1(2)} = 0 \tag{25}$$

Stage 3:

$$\bar{\mathbf{u}}^{n+1(3)} = \mathbf{u}^n + \frac{\Delta t}{2}\left(\frac{1}{Re}\nabla^2 \mathbf{u} + \mathbf{S} - \mathbf{u}\cdot\nabla\mathbf{u}\right)^{n+1(2)} \tag{26}$$

$$\nabla^2 p = 2\frac{\nabla \cdot \bar{\mathbf{u}}^{n+1(3)}}{\Delta t} \tag{27}$$

$$\mathbf{u}^{n+1(3)} = \bar{\mathbf{u}}^{n+1(3)} - \frac{\Delta t}{2}\nabla p \tag{28}$$

$$\nabla \cdot \mathbf{n}^{n+1(3)} = 0 \tag{29}$$

Stage 4:

$$\bar{\mathbf{u}}^{n+1(4)} = \mathbf{u}^n + \Delta t\left(\frac{\mathbf{F}(\mathbf{u})^n}{6} + \frac{\mathbf{F}(\mathbf{u})^{n+1(1)}}{3} + \frac{\mathbf{F}(\mathbf{u})^{n+1(2)}}{3} + \frac{\mathbf{F}(\mathbf{u})^{n+1(3)}}{6}\right) \tag{30}$$

$$\nabla^2 p^{n+1} = \frac{\nabla \cdot \bar{\mathbf{u}}^{n+1(4)}}{\Delta t} \tag{31}$$

$$\mathbf{u}^{n+1} = \bar{\mathbf{u}}^{n+1(4)} - \Delta t \nabla p^{n+1} \tag{32}$$

$$\nabla \cdot \mathbf{u}^{n+1} = 0 \tag{33}$$

where $\mathbf{F}(\mathbf{u}) = \frac{1}{Re}\nabla^2 \mathbf{u} + \mathbf{S} - \mathbf{u} \cdot \nabla \mathbf{u}$.

Spatial discretization

The previous section dealt with the temporal discretization strategy for the Navier–Stokes equations. Spatial discretization in finite element method involves the dividing of the physical domain into small elements which could be of any shape like triangles, rectangles, etc. The unknown function is assumed to have a polynomial variation within the element and is expressed in terms of the nodal variables. Depending on the type of polynomial variation desired we need to place that many nodes in each element. For our discretization we chose 4-noded isoparametric elements with equal order approximations for velocity and pressure. Finite elements offer a rich variety of elements that can be used for spatial discretization as explained very well in Huebner[19]. With this spatial discretization and use of Galerkin weighted residual formulation we arrive at a system of matrix equations as given below:

Stage 1:

$$M^D \bar{\mathbf{u}}^{n+1(1)} = M\mathbf{u}^n - \frac{\Delta t}{2}\left(K(\mathbf{u}^n)\mathbf{u}^n + \frac{1}{Re}A\mathbf{u}^n - \Omega n\right) \tag{34}$$

$$Ap = \frac{2}{\Delta t} D\bar{\mathbf{u}}^{n+1(1)} \tag{35}$$

$$M^D \mathbf{u}^{n+1(1)} = M\bar{\mathbf{u}}^{n+1(1)} - \frac{\Delta t}{2} Hp \tag{36}$$

$$H^T \mathbf{u}^{n+1(1)} = 0 \tag{37}$$

Stage 2:

$$M^D \bar{\mathbf{u}}^{n+1(2)} = M\mathbf{u}^n - \frac{\Delta t}{2}\left(K(\mathbf{u}^{n+1(1)})\mathbf{u}^{n+1(1)} + \frac{1}{Re}A\mathbf{u}^{n+1(1)} - \Omega^{n+1(1)}\right) \tag{38}$$

$$Ap = \frac{2}{\Delta t} D\bar{\mathbf{u}}^{n+1(2)} \tag{39}$$

$$M^D \mathbf{u}^{n+1(2)} = M\bar{\mathbf{u}}^{n+1(2)} - \frac{\Delta t}{2} Hp \tag{40}$$

$$H^T \mathbf{u}^{n+1(2)} = 0 \tag{41}$$

Stage 3:

$$M^D \bar{\mathbf{u}}^{n+1(3)} = M\mathbf{u}^n - \frac{\Delta t}{2}\left(K(\mathbf{u}^{n+1(2)})\mathbf{u}^{n+1(2)} + \frac{1}{Re}A\mathbf{u}^{n+1(2)} - \Omega^{n+1(1)}\right) \tag{42}$$

$$Ap = \frac{2}{\Delta t} D\bar{\mathbf{u}}^{n+1(3)} \tag{43}$$

$$M^D\mathbf{u}^{n+1(3)} = M\bar{\mathbf{u}}^{n+1(3)} - \frac{\Delta t}{2} Hp \tag{44}$$

$$H^T\mathbf{u}^{n+1(3)} = 0 \tag{45}$$

Stage 4:

$$\begin{aligned} M^D\bar{\mathbf{u}}^{n+1(4)} = M\mathbf{u}^n - \Delta t\Bigg[& 1/6\left(K(\mathbf{u}^n)\mathbf{u}^n + \frac{1}{Re} A\mathbf{u}^n - \Omega^n \right) \\ & 1/3\left(K(\mathbf{u}^{n+1(1)})\mathbf{u}^{n+1(1)} + \frac{1}{Re} A\mathbf{u}^{n+1(1)} - \Omega^{n+1(1)} \right) + \\ & 1/3\left(K(\mathbf{u}^{n+1(2)})\mathbf{u}^{n+1(2)} + \frac{1}{Re} A\mathbf{u}^{n+1(2)} - \Omega^{n+1(2)} \right) + \\ & 1/6\left(K(\mathbf{u}^{n+1(3)}\mathbf{u}^{n+1(3)} + \frac{1}{Re} A\mathbf{u}^{n+1(3)} - \Omega^{n+1(3)} \right) \Bigg] \end{aligned} \tag{46}$$

$$Ap^{n+1} = \frac{1}{\Delta t} D\bar{\mathbf{u}}^{n+1(4)} \tag{47}$$

$$M^D\mathbf{u}^{n+1} = M\bar{\mathbf{u}}^{n+1(4)} - \Delta t Hp^{n+1} \tag{48}$$

$$H^T\mathbf{u}^{n+1} = 0 \tag{49}$$

where M, K, A, D, and H are the mass, convection, diffusion, divergence, and gradient matrices, respectively. Ω results from the imposition of natural boundary conditions and the exertion of a body force. M^D is the diagonalized mass matrix obtained simply by summing across each row of the consistent mass matrix M and placing the results in the diagonal. Matrix A is a direct Galerkin finite element approximation to ∇^2. No stabilizing term is inherent in the procedure. The advantage of using this four stage Runge–Katta scheme is that the time step used can be much larger than that of the first-order projection scheme[20]. For flows which may involve high Reynolds numbers, it is beneficial to adapt this approach since a large time step is allowed.

TEST EXAMPLES

Three test cases are selected for the evaluation of the numerical accuracy of our method. They are: (1) the standing vortex problem, (2) 2D laminar flow inside a wall-driven cavity with different Reynolds number ranging from $Re=1$ to 1000, and (3) flow past a rectangular cylinder at $Re=250$. The criterion for convergence to steady state for test cases (1) and (2) was generally taken to be:

$$\frac{\|\mathbf{u}^{m+1} - \mathbf{u}^m\|_1}{\|\mathbf{u}^{m+1}\|_1} \leqslant 1.0 \times 10^{-5} \tag{50}$$

where $\|\mathbf{u}\|_1$ is the L_1 norm obtained as the sum of the absolute value of all velocity components on the interior grid multiplied by the cell size.

Standing vortex problem

The standing vortex problem is computed to verify the present formulation. This problem was introduced by Gresho[15] and was studied by Tezduyar and his research group[20] using various

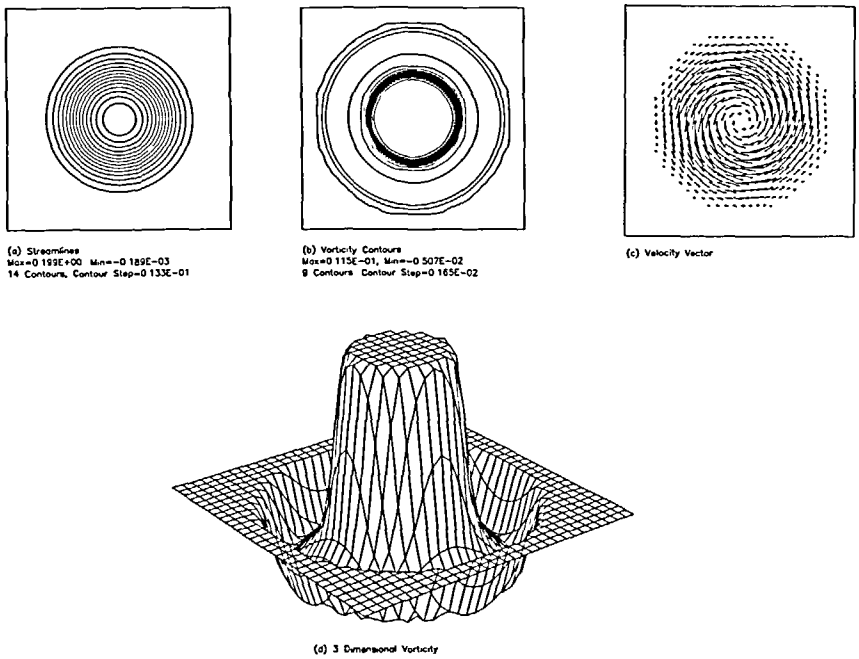

Figure 3 Standing vortex problem at $t=0$

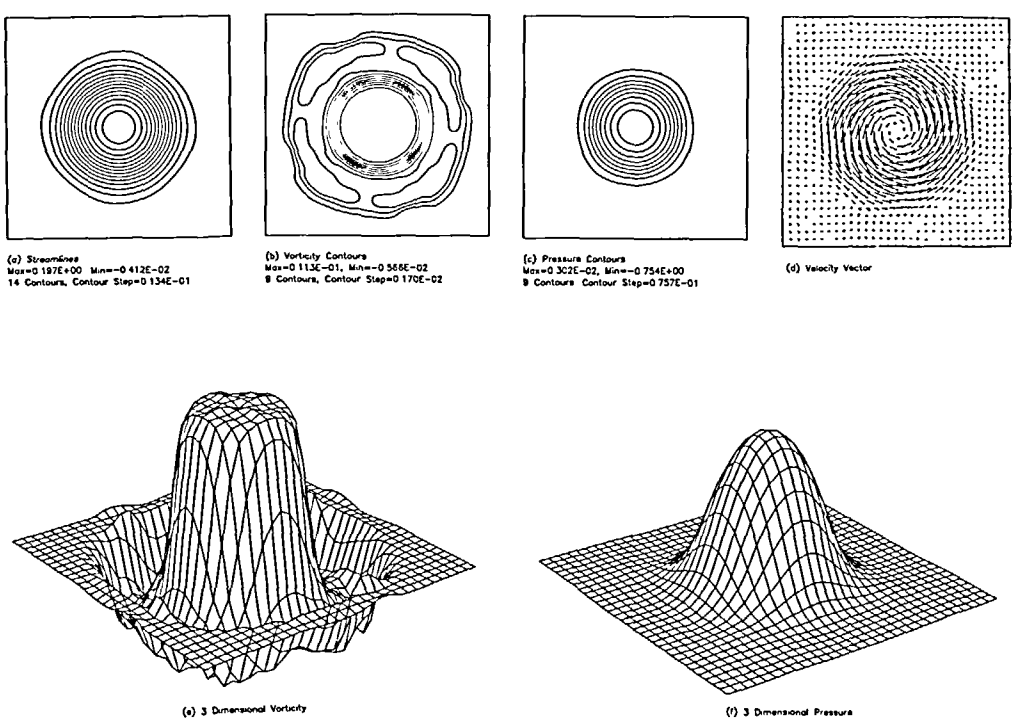

Figure 4 Solutions of the standing vortex problem at $t=3$ using Runge–Kutta method

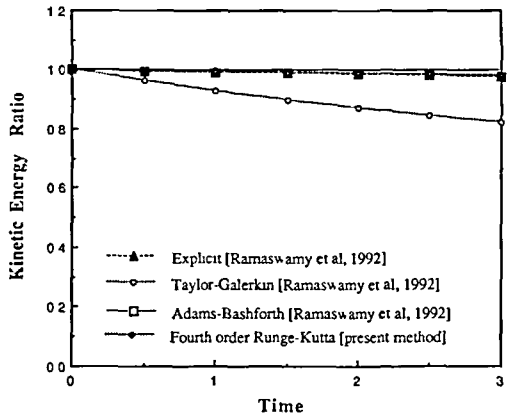

Figure 5 Time history of the vortex kinetic energy for the standing vortex problem

Table 1 Time history of the vortex kinetic energy (%)

Time	0.5	1.0	1.5	2.0	2.5	3.0
Explicit	0.996	0.991	0.987	0.983	0.980	0.977
Adams–Bashforth	0.996	0.991	0.987	0.983	0.979	0.975
Taylor–Galerkin	0.962	0.928	0.898	0.870	0.846	0.823
Runge–Kutta	0.997	0.994	0.991	0.988	0.985	0.982

theta methods. The motion of the fluid here is governed by the assumption of an ideal fluid flow in a square cavity. The initial condition (see *Figure 3*) consists of zero radial velocity and with circumferential velocity is given by $u_\theta = \{5r$ for $r<0.2$, $2-5r$ for $0.2<r<0.4$, 0 for $r>0.4\}$. The total numbers of nodal points and finite elements are 961 and 900, respectively. The computed results are shown in *Figures 4* and *5*. From these Figures it can be seen that at $t=3$, the present scheme introduces an artificial diffusion by an amount of 1.8% which is comparable to T6 formulations[20]. Finally, *Table 1* illustrates, the comparison of how much vortex kinetic energy is preserved in the domain with three other methods reported by Ramaswamy *et al.*[21] at different time levels.

2D laminar flow inside a wall-driven cavity

The second test example is the 2D laminar flow inside a wall-driven cavity. This example has been chosen to demonstrate the validity of the present computing technique with a highly non-linear effect. The computational results of the present study are compared with those of Ghia *et al.*[22] who used a multigrid finite difference method for the streamline–vorticity formulation with fine meshes.

In the present study, 40×40 elements are used with fine meshes near the walls. A pressure datum $p=0$ is specified at the middle of the bottom wall. Computed steady state velocity vectors and pressure contours are shown in *Figure 6* for Reynolds numbers 1, 100, 400 and 1000. Pressure values are given in *Table 2*. Finally, as a quantitative measure of solution accuracy, in *Table 3* we compare the properties and secondary vortices with those given in Ghia *et al.*[22], the agreement should be considered satisfactory. In this Table, we also provide the time increment Δt and CPU time to reach the same t by the other three schemes reported in Reference 21 for each *Re*.

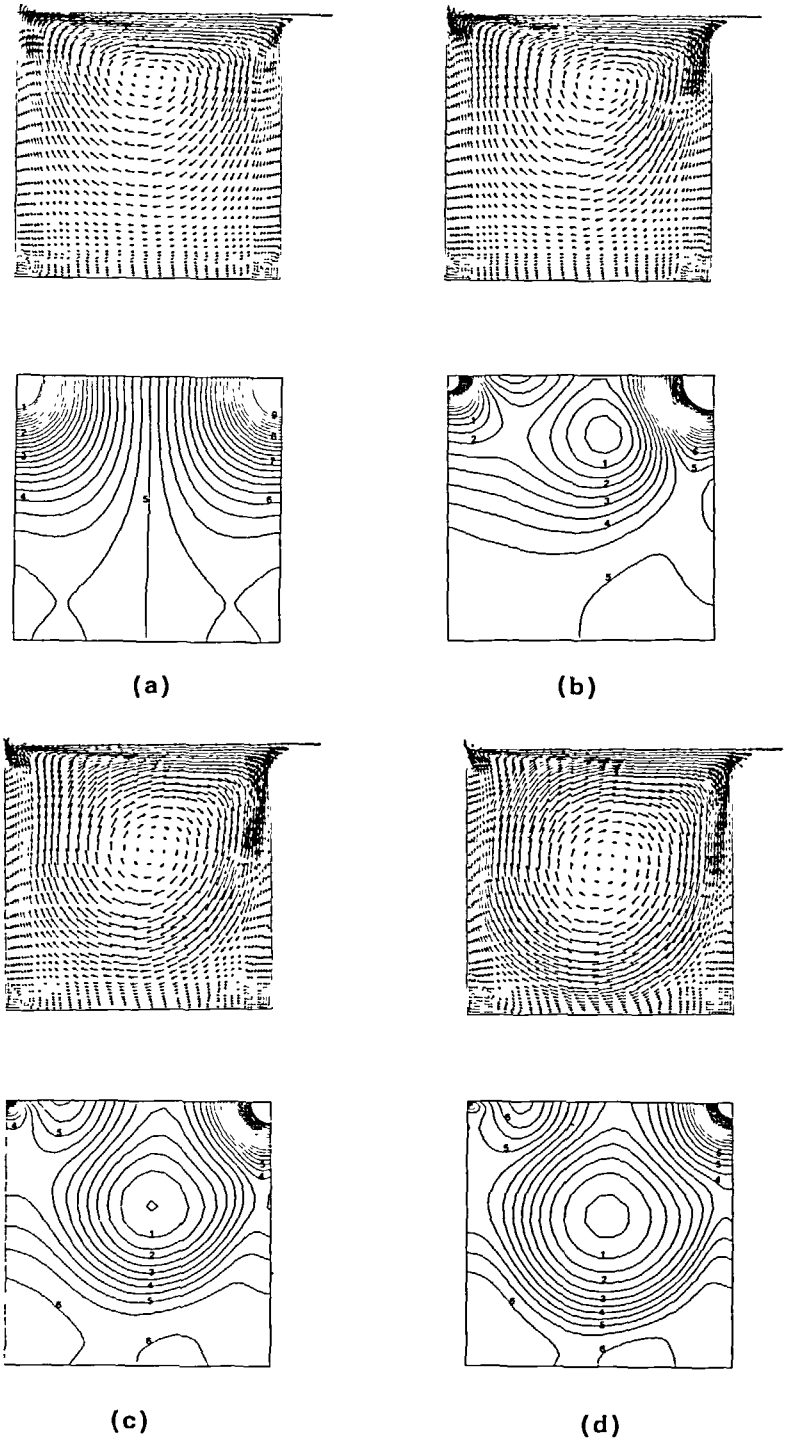

Figure 6 Steady state solutions (velocity vectors and pressure contours) for 2D laminar flow inside a wall-driven cavity: (a) $Re=1$; (b) $Re=100$; (c) $Re=400$; (d) $Re=1000$

Table 2 Values of pressure contours in *Figure 6*

Contour number	Reynolds number			
	1	100	400	1000
1	−9.60	−0.08	−0.10	−0.10
2	−6.40	−0.06	−0.08	−0.08
3	−4.00	−0.04	−0.06	−0.06
4	−1.50	−0.02	−0.04	−0.04
5	0.00	0.00	−0.02	−0.02
6	1.50	0.02	0.00	0 00
7	4.00	—	—	—
8	6.40	—	—	—
9	9.60	—	—	—

Table 3 Stream function extrema

Re	Method	Primary vortex	Bottom left '1' vortex (large) / Bottom right '1' vortex (large)	Bottom left '2' vortex (small) / Bottom right '2' vortex (small)	CPU*	Δ*t*
100	Present study	−0.103	4.60×10^{-6}	—	124.2	0.05
			1.21×10^{-5}	—		
	Ghia *et al.*	−0.103	1.75×10^{-6}	—	—	—
			1.25×10^{-5}	—		
400	Present study	−0.114	1.53×10^{-5}	—	201.5	0.05
			6.58×10^{-4}	—		
	Ghia *et al.*	−0.114	1.42×10^{-5}	—	—	—
			6.42×10^{-5}	—		
1000	Present study	−0.118	2.29×10^{-4}	—	401.7	0.05
			1.76×10^{-3}	-6.54×10^{-7}		
	Ghia *et al.*	−0.118	2.31×10^{-4}	—	—	—
			1.75×10^{-3}	-9.32×10^{-8}		

The present technique is comparable in terms of accuracy and efficiency to semi-implicit method reported in Reference 21.

Flow past a square cylinder

The above two test cases are concerned with the enclosed cavity. In this subsection numerical results for flow past a square cylinder at $Re=250$ are presented in order to verify the features of the outflow boundary procedure. The calculated results are compared with experimentally and numerically observed ones, which are reported by Davis and Moore[1]. The finite element mesh (4375 nodes and 4220 elements) and the boundary conditions are shown in *Figure 7*. At the inlet boundary, a uniform velocity distribution is assumed. The outlet boundary is assumed to be traction free. To solve the Poisson equation for pressure, the outflow boundary condition is used as described before. Along the other two boundaries, tangential tractions and the normal velocity components are assumed to be zero. The non-slip condition is prescribed at the cylinder surfaces. Plot regions for vectors and pressure contours at $t=25$ and $t=187.5$ as shown in

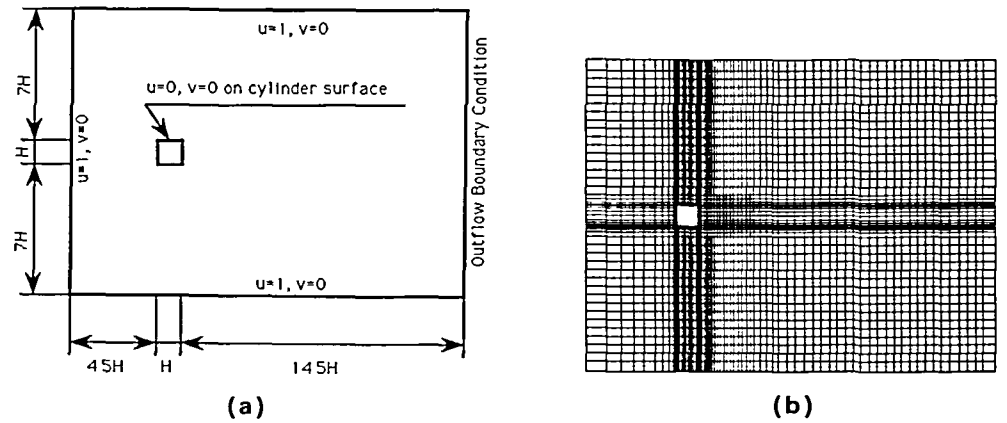

Figure 7 Flow past a rectangular cylinder: (a) problem definition; (b) finite element mesh

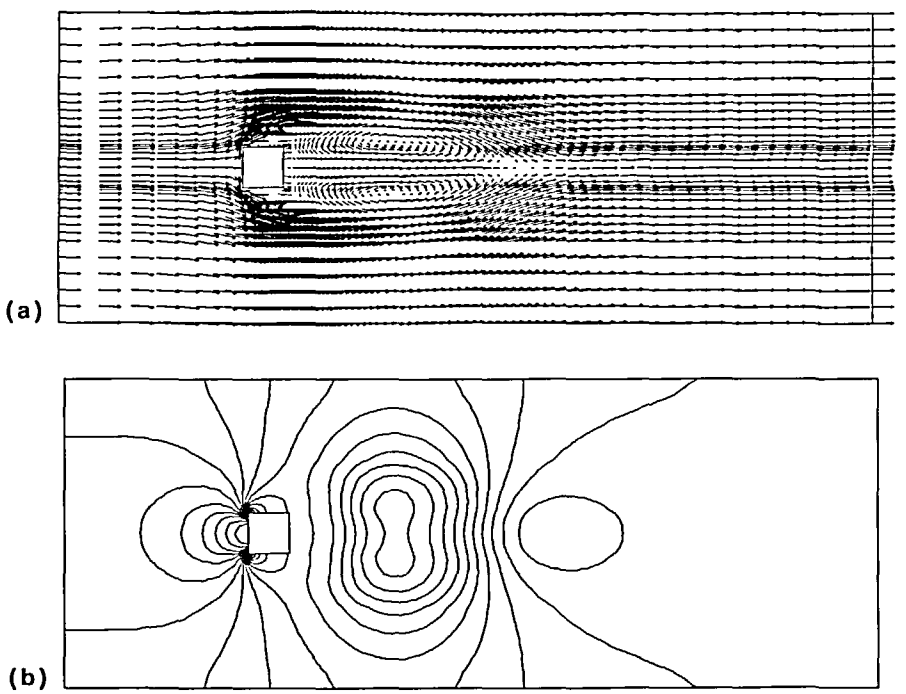

Figure 8 Development of twin vortices behind the square cylinder at $Re=250$, $t=25$: (a) velocity vectors; (b) pressure countours with $p_{min}=79.0$, $p_{max}=80.5$, and 20 equal intervals

Figures 8 and *9* are from $x=1.0$ to $x=19.0$; $y=3.7$ to $y=11.3$. In early time steps symmetric twin vortices are shown behind the cylinder. After the flow became asymmetric, a regular periodic shedding was attained at about $t=75$. In *Figure 10* variations of the drag coefficient C_D, the lift coefficient C_L and non-dimensional pressure at each centre of the cylinder sides are plotted during many cycles of periodic shedding. Finally, *Table 4* shows the comparison of the computed results with the experimental observations made by Davis and Moore[1].

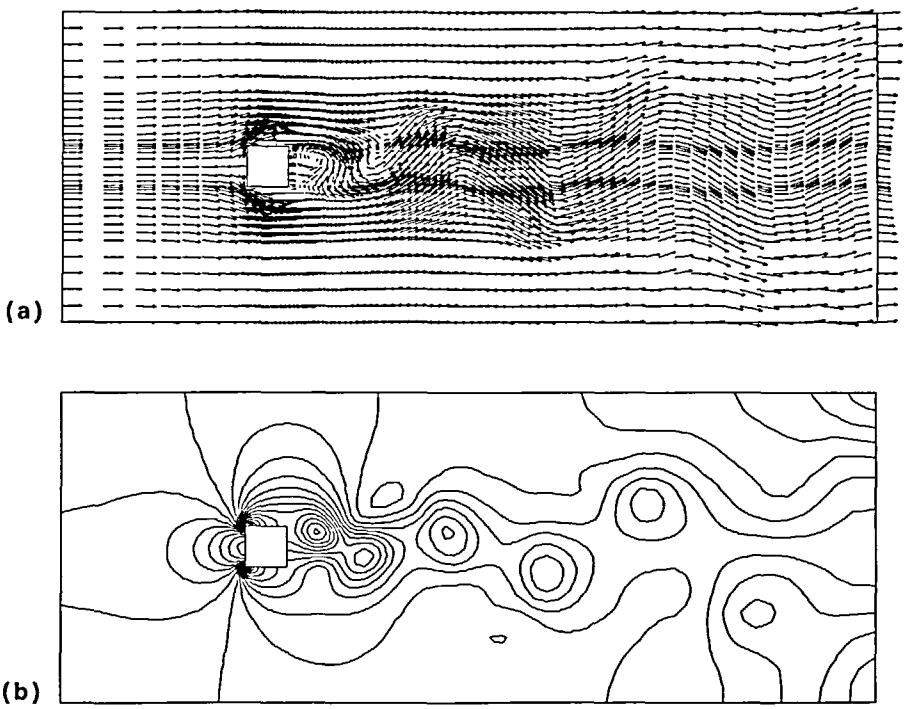

Figure 9 Velocity vectors and dimensionless pressure contours during regularly periodic shedding at $Re=250$, $t=187.5$: (a) velocity vectors; (b) pressure contours with $p_{min}=113.0$, $P_{max}=114.5$, and 20 equal intervals

NUMERICAL ANALYSIS OF EFFECTS OF SURFACE SUCTION AND BLOWING ON STROUHAL FREQUENCY

The primary objective of this investigation is to numerically determine the effects of surface suction and blowing on the St. It is also of interest to determine the slopes of the $\log St - \log(Re_0^2/Re_\infty)$ curves and to determine if the St is affected by varying Re_∞ at a constant Re_0^2/Re_∞. The fourth objective is to determine the asymptotic value of v_0 (surface velocity) at which vortex shedding becomes suppressed. Lastly, the critical value of v_0 below which ΔSt becomes negligible should also be determined. Some of these results are then compared to the theoretical predictions derived by Cohen[11]. Note that the cylinder surface velocity, v_0, is non-zero for the porous square cylinder. The results of the numerical analysis on the effects of normal surface suction and blowing on the St are summarized in *Table 5*. The Strouhal frequencies are plotted *versus* the suction and blowing velocities in *Figure 11*, while the numerically obtained $\log St - \log(Re_0^2/Re_\infty)$ relationship is shown in *Figure 12*. Discussions of the numerical results are now given separately for the suction and blowing problems.

Suction. As shown in *Table 5*, the range of suction velocity between 0.01 and 0.45 was investigated. The fully developed flow for moderate suction velocities are similar to the flow over a solid cylinder shown in *Figure 9*. *Figure 13* shows the fully developed flow for a high suction velocity of 0.4 at $t=187.5$. At this suction velocity the wake region is not as distributed as the flow with a lower suction velocity. The suction velocity of 0.4 is very close to the critical velocity at which vortex shedding becomes suppressed, which is between 0.4 and 0.45 from *Table 5*. Therefore, the flow at a suction velocity of 0.4 is almost dominated by the suction, and its

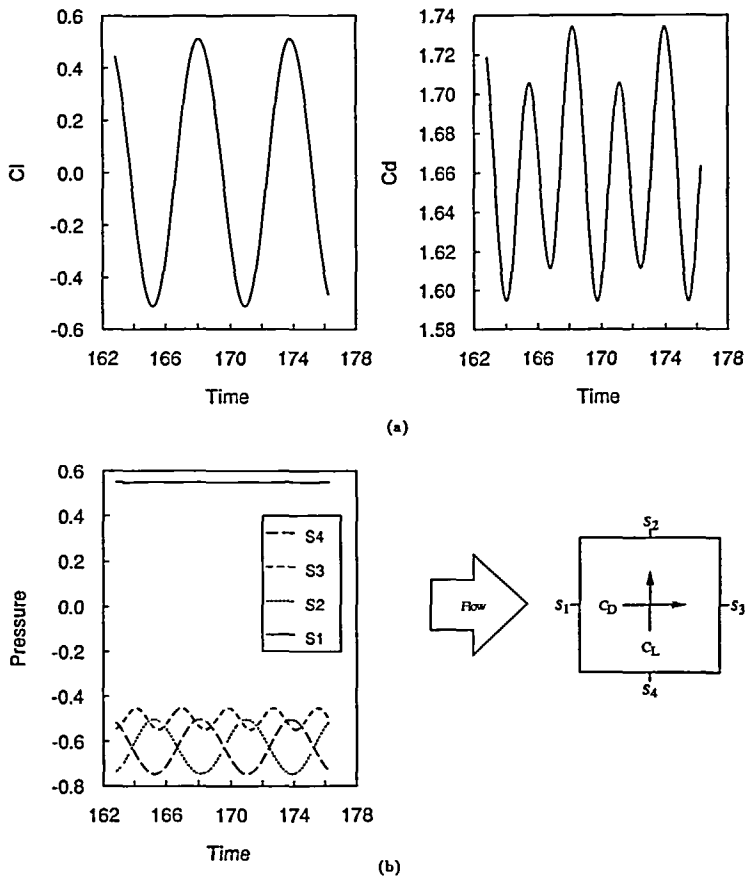

Figure 10 Time histories of: (a) the drag and the lift; (b) the surface pressures

Table 4 Some global quantities associated with vortex shedding

Source	Shedding period	Wavelength	Drag coefficient	Lift coefficient
Davis & Moore	5.9–6.3*	5.9	1.73–1.81	−0.50–0.50
Present study	5.97	5.83	1.59–1.73	−0.51–0.51

*Numerical (several meshes) and experimental

wake region becomes less affected by the shedding of vortices. *Figure 14* shows the suction dominated flow with a v_0 of 0.45 at $t=187.5$ where vortex shedding diminishes. The effect of suction on the flow velocity in the wake for downstream is negligible; here, the velocity is very close to the freestream velocity. Note that the pressure contour is symmetric.

The effect of varying Re_∞ on St while keeping Re_0^2/Re_∞ constant was determined. At a ratio of $Re_0^2/Re_\infty=2.5$, the Re_∞ was increased from 250 to 500, and the suction velocity was lowered from 0.1 to 0.007071. The increase in the St was about 3%. At a ratio of $Re_0^2/Re_\infty=22.5$, the Re_∞ was increased from 250 to 500, and the suction velocity was lowered from 0.3 to 0.21213.

Table 5 Results of effects of normal surface suction and blowing

Type of cylinder surface	Surface velocity	*St*	Period	$\frac{Re_0^2}{Re_\infty}$	$\%\Delta St^{(1)}$	C_1 amplitude	C^d range
With suction	−0.45	0	∞	50.625	−100	0	1.00
	−0.40	0.089	11.190	40	−49.4	1.58	1.28–1.72
	−0.30	0.128	7.830	22.5	−27.8	1.61	1.67–1.98
	−0.20	0.157	6.368	10	−11.2	1.39	1.77–2.15
	−0.15	0.180	5.543	5.625	+2.0	1.22	1.72–2.15
	−0.10	0.205	4.883	2.5	+15.8	1.04	1.64–2.09
	−0.05	0.206	4.845	0.625	+16.7	0.73	1.43–1.70
	−0.025	0.190	5.273	0.156	+7.3	0.53	1.43–1.58
	−0.01	0.182	5.505	0.025	+2.8	0.50	1.51–1.65
Solid	0	0.177	5.655	0	—	0.51	1.57–1.72
With blowing	0.01	0.173	5.798	0.025	−2.4	0.53	1.63–1.79
	0 025	0.166	6.030	0.156	−6.2	0.56	1.71–1.88
	0.05	0.151	6.608	0.625	−14.4	0.68	1.89–1.98
	0.10	0.142	7.043	2.5	−19.7	0.58	1.95–2.04
	0.15	0.132	7.605	5.625	−25.6	0.30	1.98–2.01
	0.20	0	∞	10	−100	0	1.86

Note: (1) $\%\Delta St$ is the % deviation of *St* from the *St* for an impermeable cylinder

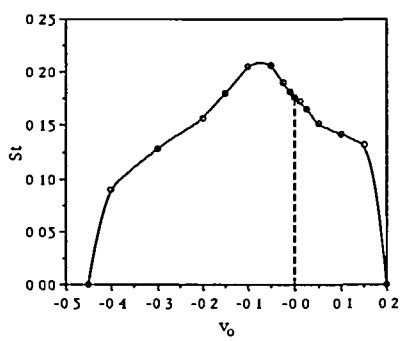

Figure 11 Strouhal frequencies *versus* suction ($-v_0$) and blowing ($+v_0$) velocities

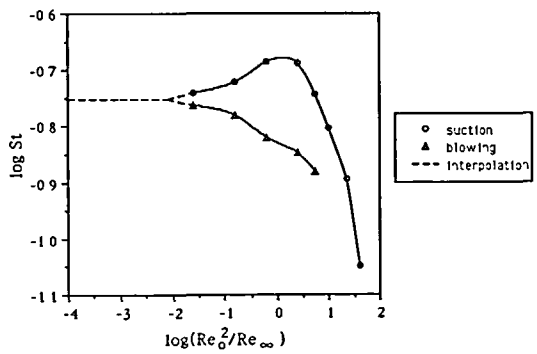

Figure 12 Numerical $\log St - \log(Re_0^2/Re_\infty)$ relationship

The increase in *St* was 28.4%. Therefore, these initial results indicate that *St* is dependent on Re_∞ at a constant ratio of Re_0^2/Re_∞. This is contradictory to the original model.

Blowing. The range of blowing velocity between 0.01 and 0.2 was investigated as shown in *Table 5*. The partly developed flow for a blowing velocity of 0.1 at $t=75$ is shown in *Figure 15*. At this stage, it is clearly seen in *Figure 15a* that the vortex shed was not immediately broken down as it is carried downstream; two separate vortices are present in the domain plotted. As the flow develops further at $t=187.5$, only one vortex is seen in *Figure 16a*. *Figure 17* shows the fully developed flow for a high blowing velocity of 0.15 at $t=247.5$. It is seen that the region close to the cylinder is dominated by the blowing process. Vortices are therefore shed not directly off of the cylinder surface but at a relatively long distance downstream. Note that a blowing velocity of 0.15 is very close to the critical velocity at which vortex shedding becomes suppressed,

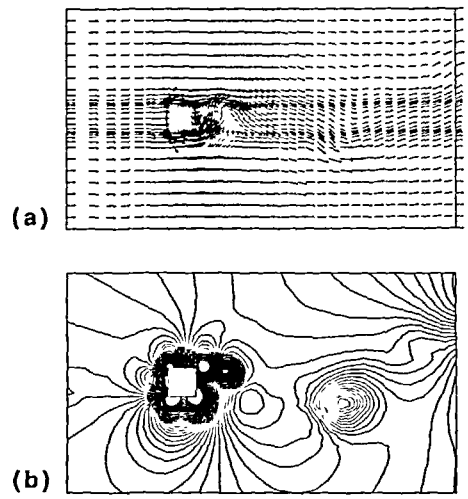

Figure 13 Fully developed flow with 0.4 suction velocity at $t=187.5$: (a) velocity vectors; (b) pressure contours with $p_{min}=16.0$, $p_{max}=17.0$, and 50 equal intervals

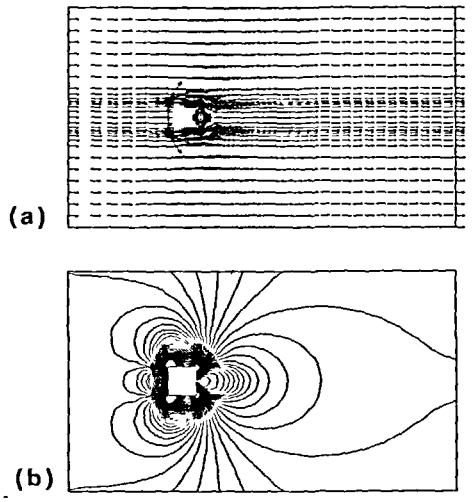

Figure 14 Fully developed flow with 0.45 suction velocity at $t=187.5$: (a) velocity vectors; (b) pressure contours with $p_{min}=45.0$, $p_{max}=46.0$, and 50 equal intervals

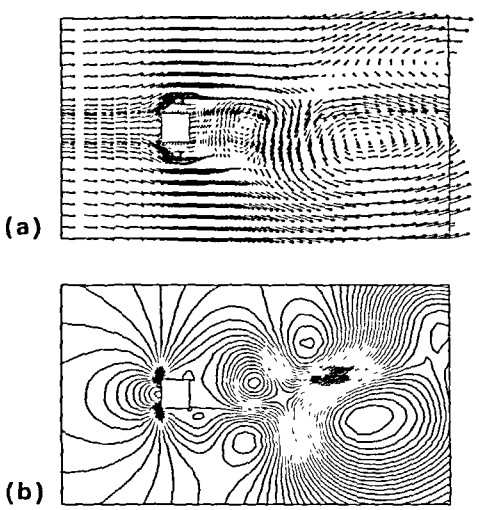

Figure 15 Fully developed flow with 0.1 blowing velocity at $t=75$: (a) velocity vectors; (b) pressure contours with $p_{min}=-67.5$, $p_{max}=-65.0$, and 50 equal intervals

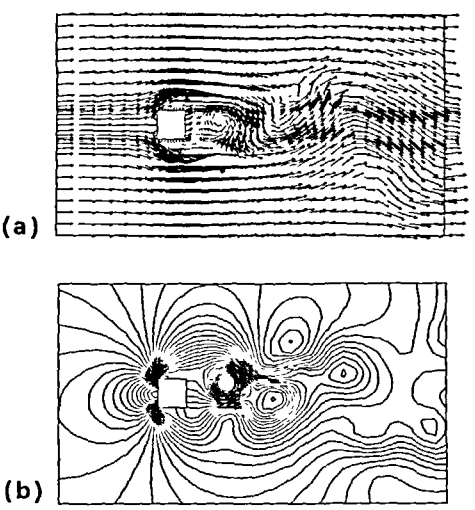

Figure 16 Fully developed flow with 0.1 blowing velocity at $t=187.5$: (a) velocity vectors; (b) pressure contours with $p_{min}=-229.0$, $p_{max}=-227.0$, and 50 equal intervals

which is determined to be between 0.15 and 0.2 from *Table 5*. At this blowing velocity of 0.15, a much longer time was required for the flow to become fully developed. *Figure 17* shows the stage where the flow had just become fully developed. When blowing velocity is further increased to 0.2, the flow field becomes totally dominated by the blowing, and vortex shedding almost disappears as seen in *Figure 18* at $t=187.5$. The effect of blowing is strong in the wake even at a distance far downstream. It can be seen that weak circulations may be present in the wake

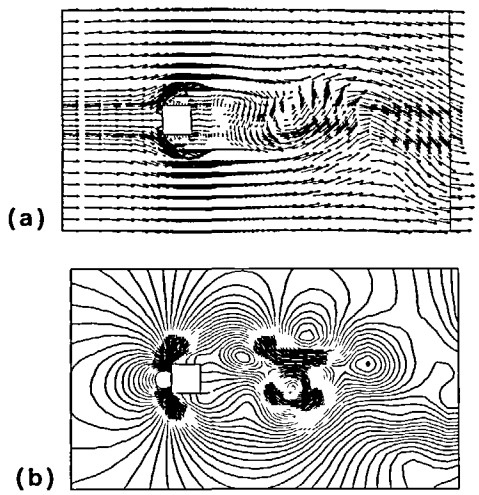

Figure 17 Fully developed flow with 0.15 blowing velocity at $t=247.5$: (a) velocity vectors; (b) pressure contours with $p_{min}=-466.25$, $p_{max}=-464.75$, and 50 equal intervals

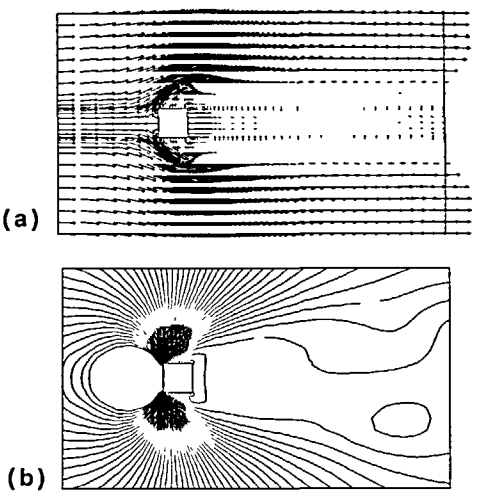

Figure 18 Fully developed flow with 0.2 blowing velocity at $t=187.5$: (a) velocity vectors; (b) pressure contours with $p_{min}=-374.5$, $p_{max}=-373.75$, and 50 equal intervals

far downstream. This is a possible cause for the pressure contour to be slightly asymmetric in the region far downstream.

The effects of varying Re_∞ on St at a constant Re_0^2/Re_∞ was determined. At a constant ratio of $Re_0^2/Re_\infty=2.5$, the Re_∞ was increased from 250 to 500, and the blowing velocity was lowered from 0.1 to 0.07071. The decrease in the St was less than 8%. At a ratio of $Re_0^2/Re_\infty=5.625$, the Re_∞ was increased from 250 to 500, and the blowing velocity was lowered from 0.15 to 0.10607. The decrease in the St is only 1%. Therefore, these initial results indicate that the effects of varying Re_∞ on the St for a particular Re_0^2/Re_∞ are only slight for the blowing problem. This agrees with the original model's prediction that St depends only on Re_0^2/Re_∞.

Comparison and discussion of the analytical and numerical solutions

The numerical results obtained in this investigation supported Cohen's theoretical prediction near the critical Re_0^2/Re_∞. As predicted, the St decreased as the blowing velocity decreases, and the St increased as the suction velocity increases. However, a limiting velocity, v_{lim}, exists for the suction problem such that, when v_{lim} is exceeded, St will begin to decrease instead of increase. The non-dimensional v_{lim} was determined to be between -0.025 and -0.1. This phenomenon is not predicted by the model. As suggested by Cohen, an upper bound exists for the suction problem where vortex shedding becomes completely suppressed. This non-dimensional upper bound v_0 was found to be between -0.4 and -0.45. For a cylinder with suction velocity greater than this, the boundary layer will have minimal thickness. Therefore, since vortex shedding originates from the boundary layer, vortex shedding will also diminish. For the St to be a continuous function of v_0, St must first decrease before reaching zero at the upper bound value of v_0. Near v_{lim}, a possible physical explanation for the increasing St to reverse and begin decreasing is that the vortex shedding may begin to overlap as v_0 increases and δ decreases. The theoretical prediction was for the vortex shedding to increase as v_0 increases. However, as the vortices are formed and shed at an increasing rate, they may begin to overlap, thus decreasing the actual shedding frequency instead of increasing it. This probably explains the initial rise followed by the decreasing behaviour of the St.

According to our computations, vortex shedding eventually disappears as the blowing velocity reaches a certain value. This is probably because a high rate of blowing causes the formation of a 'solid body', analogous to the Rankine half body (i.e. line source superposed on uniform flow) in potential flow theory. This is evident upon examining *Figure 18a*. Thus, viscous effects arising from fluid–solid wall interactions are considerably reduced, and hence, vortex shedding is eliminated altogether. As shown in *Table 5*, this non-dimensional upper bound v_0 is between 0.15 and 0.2, which is less than 20% of the freestream velocity. This shows that, for vortex shedding suppression, a much smaller v_0 is required for the blowing problem than for suction. Therefore, given a choice between surface suction or blowing for practical design applications, such as in suppressing vortex shedding, then surface blowing would be favoured over surface suction.

The change in St accelerates as v_0 increases, and the slopes of the $\log St - \log(Re_0^2/Re_\infty)$ curves are not ± 1 as predicted by Cohen. The slopes vary for different v_0, ranging from -0.05 to -0.09 for the blowing problem. For the suction problem, the slope varies from 0.02 to 0.06 for v_0 below v_{lim} and from -0.16 to -0.62 for v_0 greater than v_{lim}.

As seen in *Table 5*, the change in the St is less than $\pm 20\%$ at $Re_0^2/Re_\infty \approx 1$ which is in accordance with Cohen's prediction. If $\Delta St < 10\%$ were the criteria for the ΔSt to be considered as negligible, then the critical value of v_0 for the suction problem would fall between -0.025 and -0.05. For the flowing problem, the critical v_0 would fall between 0.025 and 0.05. Porous cylinders operating at v_0 below the critical value can then be treated as impermeable.

The $St - Re_\infty$ relationships obtained experimentally, and numerically have shown that the St characteristics for solid circular and square cylinders are not notably different. By extrapolating these results to include surface suction and blowing, it is assumed that the results for the porous cylinder and square cylinders also will not differ significantly at a low Re_∞. This was the reason why the analytical predictions were compared with the numerical results, even though different body shapes were used. However, it is important to keep in mind the future experimental results may indicate that the results are actually significantly dependent on the body shape.

Overall, by comparing the analytical and the numerical $\log St - \log(Re_0^2/Re_\infty)$ relationships plotted in *Figures 1* and *12*, fairly good agreement exists between the analytical and numerical results. The only significant difference is the unexpected decreasing portion of the curve determined numerically for suction.

CONCLUSIONS

The Runge–Kutta finite element method used in this analysis was verified by examining three test examples. The solutions were found to be in excellent agreement with existing numerical results.

The behaviour of the St for the suction and blowing problem was determined numerically. A comparison of the numerical and analytical results showed that Cohen's boundary layer growth and collapse model of vortex shedding appears to successfully predict the deviation of the St (from the impermeable case) near the critical Re_0^2/Re_∞, i.e. suction tends to increase the St, whereas blowing decreases it. The model, however, fails grossly at larger values of Re_0^2/Re_∞. For the suction problem, the following conclusions were formed:

1. St increases with increasing suction for v_0 below v_{lim} determined to be between -0.025 and -0.1. At v_0 beyond v_{lim}, St will decrease with increasing suction.
2. The asymptotic value of v_0 at which vortex shedding is suppressed is determined to be between -0.4 and -0.45.
3. Letting $\Delta St < 10\%$ be the criteria for negligible change in St, the critical value of v_0 would fall between -0.025 and -0.05 (for v_0 below v_{lim}). Cylinders with surface suction velocities less than this critical v_0 can then be treated as impermeable.

4. St is dependent on Re_∞ at a constant ratio of Re_0^2/Re_∞.
5. The slope of the $\log St - \log(Re_0^2/Re_\infty)$ curve ranges from 0.02 to 0.06 for v_0 below v_{lim} and from -0.16 to -0.62 at v_0 greater than v_{lim}. The change in St accelerates as v_0 increases.

For the blowing problem, the following conclusions were made:

1. St decreases with increasing blowing.
2. The asymptotic value of v_0 at which vortex shedding is suppressed is determined to be between 0.15 and 0.2.
3. Letting $\Delta St < 10\%$ be the criteria for negligible change in St, the critical value of v_0 would fall between 0.025 and 0.05. Cylinders with surface blowing velocities less than this critical v_0 can then be treated as impermeable.
4. For the same value of Re_0^2/Re_∞, the St will decrease slightly as Re_∞ increases.
5. The slope of the $\log St - \log(Re_0^2/Re_\infty)$ curve ranges from -0.05 to -0.09. The change in St accelerates as v_0 increases.

REFERENCES

1 Davis, R. and Moore, E. A numerical study of vortex shedding from rectangles, *J. Fluid Mech.*, **116**, 475–506 (1982)
2 Okajima, A., Nagahisa, T. and Rokugoh, A. A numerical analysis of flow around rectangular cylinders, *JSME Int. J. (Series II)*, **33**, 702–711 (1990)
3 Okajima, A. Strouhal numbers of rectangular cylinders, *J. Fluid Mech.*, **123**, 379–398 (1982)
4 Shimura, M. and Kawahara, M. Two dimensional finite element flow analysis using the velocity correction method, *JSCE Struct. Eng./Earthqu. Eng.*, **5**, 255–263 (1988)
5 Yoshida, Y. and Nomura, T. A transient solution method for the finite element incompressible Navier–Stokes equations, *Int. J. Num. Meth. Fluids*, **5**, 873–890 (1985)
6 Rothberg, R. A numerical study of vortex shedding suppression in laminar flow about a cylinder near a plane boundary, *PhD Thesis*, Rice University, Houston (1989)
7 Briscolini, M. and Santangelo, P. Development of the mask method for incompressible unsteady flows, *J. Comput. Phys.*, **84**, 57–75 (1989)
8 Tezduyar, T. E. and Shih, R. Numerical experiments on downstream boundary of flow past cylinder, *J. Eng. Mech.*, **117**, 854–871 (1991)
9 Tanahashi, T. and Okanaga, H. GSMAC finite element method for unsteady incompressible Navier–Stokes equations at high Reynolds numbers, *Int. J. Num. Meth. Fluids*, **11**, 479–499 (1990)
10 Tabata, M. and Fujima, S. An upwind finite element scheme for high Reynolds number flows, *Int. J. Num. Meth. Fluids*, **12**, 305–322 (1991)
11 Cohen, R. D. Predicting the effects of surface suction and blowing on the Strouhal frequencies in vortex shedding, *JSME Int. J., (Series II)*, **34**, 30–39 (1991)
12 Chorin, A. J. Numerical solution of the Navier–Stokes equations, *Math. Comput.*, **22**, 745–762 (1968)
13 Ku, H. C., Hirsh, R. S., Taylor, T. D. and Rosenberg, A. P. A pseudospectral matrix element method for solution of three-dimensional incompressible flows and its parallel implementation, *J. Comput. Phys.*, **83**, 260–291 (1989)
14 Anderson, C., Greengard, C., Greengard, L. and Rokhlin, V. On the accurate calculation of vortex shedding, *Phys. Fluids (A)*, **2**, 9883–885 (1990)
15 Gresho, P. M. and Chan, S. T. Semi-consistent mass matrix techniques for solving the incompressible Navier–Stokes equations, *Preprint UCRL-99503* (1988)
16 Zienkiewicz, O. C. Incompressibility without tears—how to avoid restrictions of mixed formulation, personal communication
17 Chorin, A. J. A numerical method for solving viscous incompressible flow problems, *J. Comput. Phys*, **2**, 12–26 (1967)
18 Harlow, F. H. and Welch, J. E. Numerical calculation of time-dependent viscous incompressible flow of fluid with free surface, *Phys. Fluids*, **8**, 2182–2189 (1965)
19 Huebner, K. H. *The Finite Element Method for Engineers*, 2nd Edn, John Wiley, New York (1982)
20 Tezduyar, T. E., Liou, J. and Ganjoo, D. K. Incompressible flow computations based on the vorticity–stream function and velocity–pressure formulations, *Comp. Struct.*, **35**, 445 (1990)
21 Ramaswamy, B., Jue, T. C. and Akin, J. E. Semi-implicit and explicit finite element schemes for coupled fluid/thermal problems, *Int. J. Num. Meth. Eng.*, **34**, 675–696 (1992)
22 Ghia, U., Ghia, K. N. and Shin, C. T. High-*Re* solutions for incompressible flow using the Navier–Stokes equations and a multigrid method, *J. Comput. Phys.*, **48**, 387–411 (1982)